Characterizing the as-built surface topography of Inconel 718 specimens as a function of laser powder bed fusion process parameters

Bart Raeymaekers

Department of Mechanical Engineering, Virginia Tech, Blacksburg, Virginia, USA, and

Thomas Berfield

Department of Mechanical Engineering, University of Louisville, Louisville, Kentucky, USA

Abstract

Purpose – The ability to use laser powder bed fusion (LPBF) to print parts with tailored surface topography could reduce the need for costly post-processing. However, characterizing the as-built surface topography as a function of process parameters is crucial to establishing linkages between process parameters and surface topography and is currently not well understood. The purpose of this study is to measure the effect of different LPBF process parameters on the as-built surface topography of Inconel 718 parts.

Design/methodology/approach – Inconel 718 truncheon specimens with different process parameters, including single- and double contour laser pass, laser power, laser scan speed, build orientation and characterize their as-built surface topography using deterministic and areal surface topography parameters are printed. The effect of both individual process parameters, as well as their interactions, on the as-built surface topography are evaluated and linked to the underlying physics, informed by surface topography data.

Findings – Deterministic surface topography parameters are more suitable than areal surface topography parameters to characterize the distinct features of the as-built surfaces that result from LPBF. The as-built surface topography is strongly dependent on the built orientation and is dominated by the staircase effect for shallow orientations and partially fused metal powder particles for steep orientations. Laser power and laser scan speed have a combined effect on the as-built surface topography, even when maintaining constant laser energy density.

Originality/value — This work addresses two knowledge gaps. (i) It introduces deterministic instead of areal surface topography parameters to unambiguously characterize the as-built LPBF surfaces. (ii) It provides a methodical study of the as-built surface topography as a function of individual LPBF process parameters and their interaction effects.

Keywords Laser powder bed fusion (LPBF), As-built surface topography, Interaction effects

Paper type Research paper

1. Introduction

Laser powder bed fusion (LPBF) is an additive manufacturing (AM) technology in which a laser selectively melts and fuses metal powder particles in a layer-by-layer fashion to manufacture three-dimensional (3D), free-form metal parts (Gibson *et al.*, 2014). LPBF enables manufacturing parts with intricate internal and external geometry that is difficult or even impossible to manufacture with traditional subtractive or formative manufacturing processes. Consequently, LPBF offers design flexibility, allows for mass-customization of parts and minimizes material waste, thus making it an attractive process to manufacture complex-geometry, high-value parts for use in, e.g. aerospace (Blakey-Milner *et al.*, 2021; Kerstens *et al.*, 2021), automotive (Leal *et al.*, 2017; Vasco, 2021) and medical device (Puppi and Chiellini, 2020; Singh and Ramakrishna, 2017) industries.

The current issue and full text archive of this journal is available on Emerald Insight at: https://www.emerald.com/insight/1355-2546.htm



However, LPBF parts typically require post-processing to improve their mechanical properties and modify as-built surface topography prior to use in engineering applications (Bourell et al., 2017; Kruth et al., 1998; Peng et al., 2021). As a result, extensive literature is available on different post-processing methods [see, e.g Peng et al. (2021); Xu et al. (2021)]. Here, we focus on the as-built surface topography of LPBF parts, which defines functional contact, traction, friction, and wear when interacting with other components, e.g. after assembly in engineering applications (Raeymaekers, 2022; Joe et al., 2022).

Several methods exist to post-process the as-built surface topography of LPBF parts. For instance, machining and superfinishing modify the as-built surface topography by removing material (Nakayama and Hashimoto, 1995; Kumbhar and Mulay, 2018), whereas hot isostatic pressing (Jiang *et al.*, 2019; du Plessis and Rossouw, 2015; Essa *et al.*, 2018; Tillmann *et al.*, 2017) and annealing (Newell *et al.*, 2019) reduce porosity

Declaration of competing interest.

The authors declare no competing interests.

Received 5 May 2024 Revised 13 August 2024 Accepted 11 September 2024

Volume 31 · Number 1 · 2025 · 200-217

and surface roughness by means of compression (Tian et al., 2020). Chemical treatment (Mohammadian et al., 2018; Pyka et al., 2013) removes partially fused metal powder particles from as-built surfaces, and mechanical post-processing such as shot peening reduces surface roughness through mechanical impact (Calignano et al., 2013; Lesyk et al., 2020). Nevertheless, post-processing is time-consuming and costly, and it is sometimes impractical or technically infeasible to modify the as-built surface topography of complex or internal features such as lattice structures. Hence, reducing or even eliminating post-processing of the as-built surfaces of LPBF parts is a significant engineering problem, which becomes increasingly important when transitioning LPBF from a rapid prototyping technology to a manufacturing process.

One possible solution to reducing or eliminating postprocessing of the as-built surfaces is to tune the LPBF process to print parts with tailored as-built surface topography. However, this solution requires intricate knowledge of the relationship between the LPBF process parameters and the corresponding as-built surface topography. In turn, this approach requires the ability to accurately measure and characterize the surface topography of as-built LPBF surfaces.

Thus, researchers have measured and characterized as-built LPBF surface topography using different techniques, including optical profilometry, confocal laser scanning microscopy, and scanning electron microscopy (SEM) (Lou et al., 2019; Townsend et al., 2016). The as-built surface topography displays distinct features inherent to the LPBF process, which sometimes span multiple length scales, including partially fused metal powder particles (Carter et al., 2022; Sendino et al., 2023), laser scan lines (Paraschiv et al., 2022), "staircase" effect (Yasa et al., 2016), pores (Valente et al., 2019), and globule formations that result from so-called "balling" (Li et al., 2012) (see Section 2.3 for a description of these different surface topography features). The choice of measurement technique and measurement parameters, which determine the vertical and lateral resolution as well as the field-of-view, depends on the purpose of the measurement and the topography features and length scales one intends to measure and characterize (Newton et al., 2019). For instance, Lou et al. (Lou et al., 2019) measured the as-built surface topography of LPBF surfaces and used Gaussian filters and watershed segmentation to characterize low-frequency waviness features such as laser scan lines and high-frequency roughness features such as partially fused metal powder particles and pores. Their results emphasize the importance of segregating distinct surface topography features when characterizing the asbuilt surface topography of LPBF parts.

Several research groups have also attempted to quantify the relationship between as-built surface topography and LPBF process parameters, including laser power, laser scan speed, layer thickness, build orientation, and metal powder characteristics. Tian *et al.* (2017) investigated the effect of laser scan speed, laser power, and build orientation on the mean surface roughness *Ra* of several stylus traces of the as-built surface. They measured that *Ra* of up-skin surfaces is independent of the laser process parameters, whereas *Ra* of down-skin surfaces decreases with increasing laser scan speed and laser power. In contrast, Strano *et al.* (2013) measured a higher *Ra* value for up-skin than for down-skin as-built surfaces. *R*-parameters, such as *Ra*, are based

on one or multiple traces of the surface, whereas areal surface topography parameters (*S*-parameters) are calculated over an area [ISO 25178-2:2021(En), 2021].

Narasimharaju et al. (2021) examined the effect of build orientation during LPBF on the as-built surface topography using areal surface topography parameters, including mean surface roughness Sa, root mean square (RMS) surface roughness Sq, skewness Ssk, and kurtosis Sku. They measured a higher Sa and Sq for the down-skin than for the up-skin as-built surface topography, which contrasts results by both Tian et al. (2017) and Strano et al. (2013). They also observed a positive skewness Ssk for both up-skin and down-skin as-built surfaces, which indicates a prevalence of peaks as opposed to valleys. Furthermore, they determined that the "staircase" effect, which results from approximating inclined or curved surfaces with discrete layers, has a dominant effect on Sa and Sq relative to that of other surface topography features such as partially fused metal powder particles. Cabanettes et al. (2018) considered the effect of print direction on the as-built surface topography using Ra, Sa, Sq, and Ssk. In contrast to Narasimharaju et al. (2021), they determined that a negative and positive skewness Ssk distinguishes a down-skin from an up-skin as-built surface, respectively. Whip et al. (2019) quantified Ra, Rsk, Rku, Rp, Rv, Sa, Ssk, Sku, Sp, and Sv to analyze the effect of combined (instead of single parameter) variations of laser power and laser scan speed on the as-built surface topography, and they presented maps that depict the variations of these surface topography parameters as a function of laser power and laser scan speed. A few papers have also documented that tuning the parameters of a single contour laser pass can reduce the surface roughness of the as-built surfaces (Tian et al., 2017; Snyder and Thole, 2020; Yang et al., 2019).

Surface topography also relates to mechanical properties, in particular fatigue life (Raeymaekers, 2022). For instance, Gockel et al. (2019) linked fatigue life of specimens manufactured with LPBF to as-built surface topography to optimize process parameters in terms of maximum fatigue life. They determined that maximum valley depth Sv decreases with increasing laser power and increases with increasing laser scan speed, and they measured that fatigue life is inversely related to Sv, but no substantial correlation exists with Sa. Similarly, Watring et al. (2019) showed that fatigue life of IN718 specimens shows weak correlation with Sa.

Experimentally determining the relationship between LPBF process parameters and the as-built surface topography parameters through methodical studies or trial-and-error does not always lead to optimal results or descriptive models because the number of parameter combinations one can experimentally evaluate is practically limited due to economical constraints. Thus, several research groups have also attempted to capture the relationship between LPBF process parameters and the asbuilt surface topography in predictive models, including regression models and data-driven models derived from machine learning (ML) algorithms. For instance, Cao et al. (2021) developed a data-driven model using a Kriging approach to estimate the as-built surface topography parameters as a function of laser power, laser scan speed, and melt pool temperature. Alternatively, Özel et al. (2019) used an artificial neural network to relate laser power during the LPBF process with several as-built surface topography parameters,

Volume 31 · Number 1 · 2025 · 200-217

including Sa, Sq, Ssk, and Sku. Similarly, Detwiler et al. (2022) used multivariate regression, and Detwiler and Raeymaekers (2022) implemented various interpretable and non-interpretable ML algorithms to derive data-driven models that link as-built surface topography parameters to LPBF process parameters. They specifically compared the prediction accuracy of these models when using several areal, statistical, and deterministic surface topography parameters, and they showed that deterministic surface topography parameters relate most closely to the LPBF process parameters.

However, we identify two knowledge gaps from these prior studies. First, almost all studies quantify the surface topography using areal surface topography parameters, likely because these parameters are well-known, widely adopted in standards and straightforward to calculate from optical or stylus profilometry measurements [ISO 25178-2:2021(En), 2021]. Yet, it is well-known that they do not unambiguously quantify the surface topography (Mate and Carpick, 2019), and, thus, their interpretative value is questionable when surfaces display similar areal topography parameter values but also qualitatively show distinct surface topography features, or vice versa. Second, existing works consider the effect of individual process parameters on the as-built surface topography, but neglect potentially important interaction effects between multiple LPBF process parameters.

This work aims to address these knowledge gaps. Hence, we characterize the as-built surface topography of Inconel 718 specimens as a function of LPBF process parameters, including single- and double-contour laser pass, laser power, scan speed, and build orientation, using both deterministic and areal surface topography parameters. Furthermore, we methodically evaluate the effect of individual process parameters and their interactions on the as-built surface topography and link it to the underlying process physics, informed by the surface topography data. Finally, we formulate recommendations to obtain specific as-built surface topography by tuning LPBF laser parameters and build orientation.

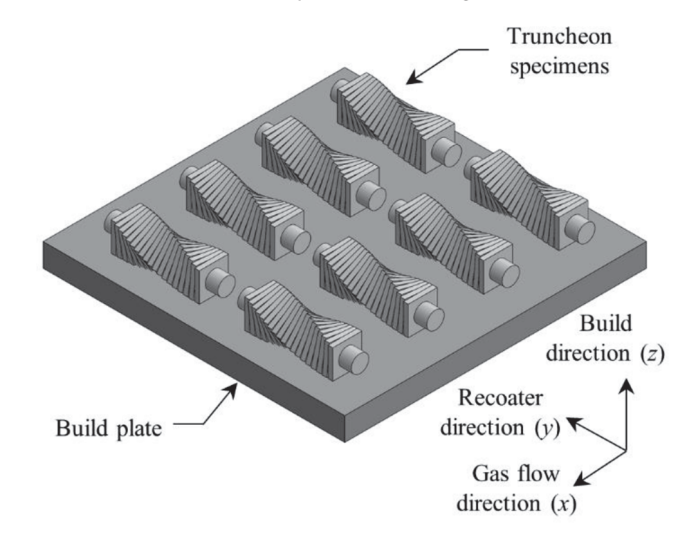
2. Materials and methods

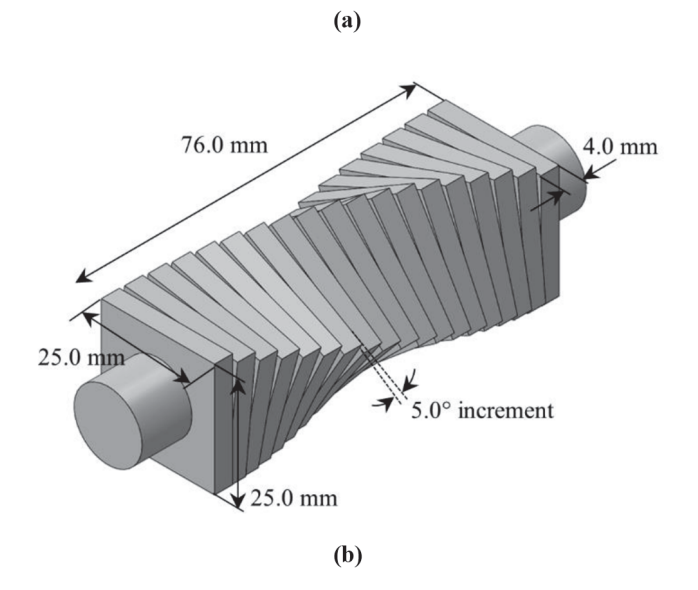
2.1 Manufacturing truncheon specimens

We use an EOS M290 LPBF printer to manufacture 16 truncheon specimens with virgin Inconel 718 (IN718) powder (Praxair, $26.2\,\mu\text{m}$ avg. diameter). Figure 1(a) schematically shows the build plate with the location of the truncheon specimens and the LPBF process directions, including build-, recoater-, and gas flow-directions. We fit eight truncheon specimens per build plate and, thus, require two build plates that each take approximately 40 h to complete. Figure 1(b) shows a schematic of a single truncheon specimen and its dimensions; it comprises 19 individual $25\,\text{mm} \times 25\,\text{mm} \times 4\,\text{mm}$ squares, whose build orientation $0^{\circ} \le \alpha \le 90^{\circ}$ changes in 5° increments. In the absence of an established standard, the truncheon geometry is similar to the one used previously by others (Strano et al., 2013; Narasimharaju et al., 2021).

We use the standard EOS-recommended settings for IN718, including a layer thickness of 40 μ m and a hatch offset of 15 μ m, and maintain constant bulk hatching laser process parameters for all truncheon specimens because we specifically focus on the as-built surface topography, which is almost entirely determined by the contour laser parameters.

Figure 1 (a) Schematic of the build plate layout, showing the placement of the truncheon specimens and the LPBF process directions; (b) schematic of a truncheon specimen, indicating its dimensions





Source: Figure by authors

Hence, we use two sets of contour laser process parameters, both intended to minimize the surface roughness of the as-built surfaces and facilitate fully dense bonding with the interior hatched region of the component (Artzt et al., 2020; Karimialavijeh et al., 2023). The contour laser pass(es) trace(s) the edges of each layer after the hatched region has completed, thereby slightly covering part of the interior hatch pattern that fills the bulk of each layer. In general, up-skin surfaces use multiple contour laser passes with high laser power, whereas down-skin surfaces mostly use a single laser contour pass with low power because the latter are supported by unsintered powder in the contour region instead of previously sintered metal layers that act as a heat sink.

The "Contour 2" parameters define the standard, outermost part contour laser pass, whereas the "Contour 1" parameters provide additional smoothing along the contours of the part

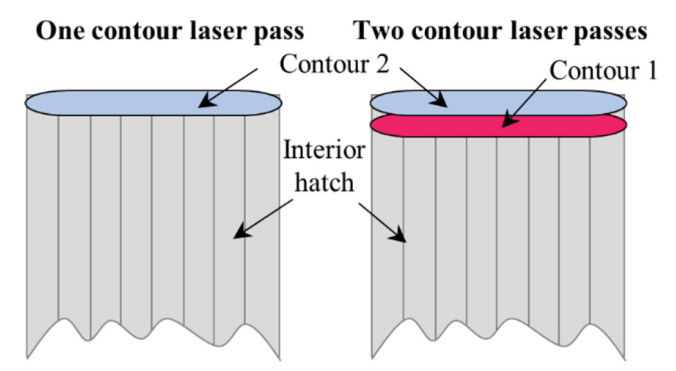
Volume 31 · Number 1 · 2025 · 200-217

geometry, by means of an additional contour laser pass that partially overlaps with the outermost contour laser pass (Paraschiv *et al.*, 2022; Kafka *et al.*, 2023). When using two contour laser passes, Contour 1 (innermost) occurs before Contour 2 (outermost). The offset between both contour laser passes is a tunable parameter but remains constant at $12 \mu m$ in this work (EOS-recommended settings for IN718). Figure 2 schematically illustrates the geometry of one (Contour 2) versus two (Contour 2 and 1) contour laser passes and shows that the area covered by two contour laser passes exceeds that of one contour laser pass, thus providing additional smoothing of the as-built surface topography.

To implement a methodical study design, we disable separate conditional process parameters for up-skin and downskin surfaces. Instead, we maintain constant LPBF process parameters for each individual truncheon specimen, i.e. we use the same contour laser parameters within a single truncheon specimen regardless of up-skin or down-skin condition. Truncheon specimens 1–6 implement contour laser parameter variations around the EOS-recommended settings for down-skin surfaces, whereas truncheon specimens 7–16 use parameter variations about the EOS-recommended settings for up-skin surfaces. Table 1 lists the LPBF process parameters for each truncheon specimen. Note that specimens 2 and 5 as well as 9 and 14 use the same LPBF process parameters but were manufactured on a different build plate.

EOS defines the optimal contour laser power and laser scan speed for IN718 as 35 W and 2,000 mm/s (Contour 2) and 138 W and 390 mm/s (Contour 1). We adjust the optimal process parameters in the experiments upward and downward by 10% and 20%, respectively. Varying the process parameters even more could compromise the ability to fuse the metal powder or cause overheating of the melt pool (Brown et al., 2018; Huynh et al., 2022). The experiment design includes a comparison between specimens 1–6 and 7–16 that use a single-and double-contour laser pass, respectively. Furthermore, specimens 7–11 implement variations of the contour laser power with a constant laser scan speed, whereas specimens 12–16 implement variations of the contour laser scan speed with constant laser power. Hence, the methodical experiment design enables comparing the effect of changing individual as well as

Figure 2 Top-view layer schematic of one and two contour laser passes, showing that the contour laser covers part of the interior hatch pattern by tracing the contours of each layer



Source: Figure by authors

combinations of LPBF process parameters on the as-built surface topography. Since we focus on measuring and characterizing the as-built surface topography, we do not postprocess the truncheon specimens.

2.2 Measuring as-built surface topography

Surface topography measurements quantify the surface height zas a function of discrete coordinate locations x, y on the surface, i.e. z = f(x,y), to create a surface topography map from which we derive surface topography parameters that describe the surface topography features and characteristics (Leach, 2011). We measure the surface topography with a white light interferometer (WLI) (Contour X-500, Bruker, Tucson, AZ), using vertical scanning interferometry mode and 10X optical zoom, which results in a field-of-view of 1,200 pixels × 1,000 pixels, with $0.38 \,\mu m$ lateral and $1-5 \,nm$ vertical resolution. These measurement parameters result from a convergence study in which we selected four different truncheon specimens and performed trial measurements for five different build orientations on each specimen, incrementally increasing the field-of-view until the mean surface roughness Sa did not change more than 5% for all specimens and build orientations. We seamlessly stitch together a square array of 3×3 measurements to increase the field-of-view to $1.8 \times 1.8 \,\mathrm{mm}$, which enables capturing the specific features that are characteristic of as-built LPBF surfaces. For each surface topography measurement, we correct for specimen tilt, set the centerline average to zero and use the Bruker data-restoration function to fill-in a maximum of 5% missing pixels based on a Gaussian filter. Missing pixels are the result of limited reflectivity and coarse topography of the as-built surfaces.

Figure 3(a) shows a typical truncheon specimen and identifies the up-skin and down-skin surfaces, in addition to the locations on each individual square of the truncheon specimen where we measure the surface topography (maroon-colored markers). A magnified inset image depicts the as-built surface topography. In addition, Figure 3(b) shows a typical surface topography map that results from a WLI measurement. We perform the surface topography measurements in arbitrary order to avoid operator bias and measure the surface topography of each of the 19 as-built surfaces of each of the 16 truncheon specimens once, i.e. a total of $19 \times 16 = 304$ surface topography measurements. We only consider up-skin surfaces in this work because it is difficult to remove the IN718 support structures from the down-skin surfaces without altering the as-built surface topography.

2.3 Characterizing as-built surface topography

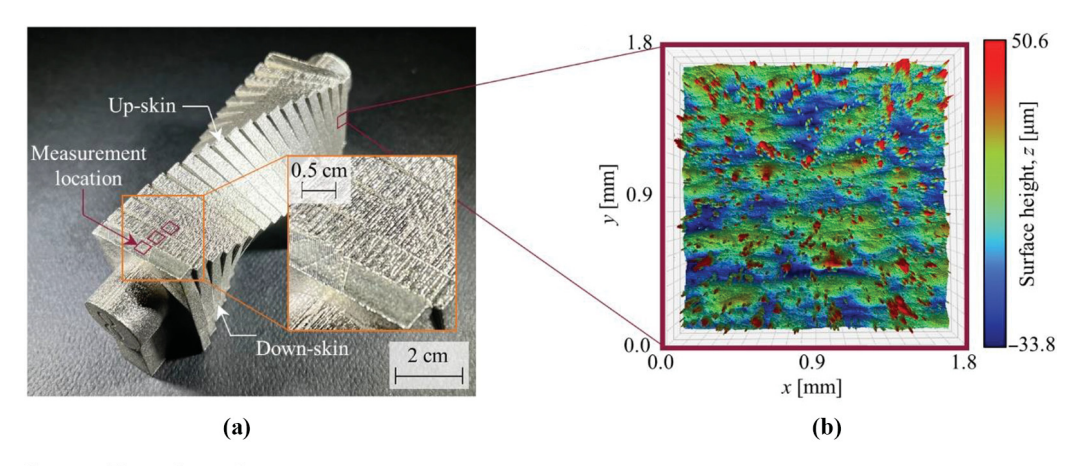
Figure 4(a) illustrates the layer-by-layer LPBF process to manufacture surfaces under different build orientations ($\alpha_1 < \alpha_2$) by stacking layers like a staircase in the build direction, thus approximating the surface inclination by means of discrete stairsteps. The size of the stairsteps decreases with increasing build orientation α , i.e. $\Delta d_1 > \Delta d_2$. The contour laser pass traces the perimeter of each layer, and, thus, they appear as parallel raised structures in the as-built surface topography, which is often referred to as the "staircase effect." For instance, Figure 4(b) shows a surface topography measurement of an asbuilt surface manufactured with a build orientation $\alpha = 5^{\circ}$. Considering a layer thickness of 40 μ m, the flat surface under

Volume 31 · Number 1 · 2025 · 200–217

Table 1 LPBF process parameters for each truncheon specimen, showing contour laser power and scan speed. Linear energy density is based on the laser scan speed, whereas volume energy density additionally accounts for layer thickness

	Contour 1 (additional)				Contour 2 (standard)			
		Laser energy density				Laser energy density		
Specimen	Power [W]	Speed [mm/s]	Linear [Ws/mm]	Volume [Ws/mm ²]	Power [W]	Speed [mm/s]	Linear [Ws/mm]	Volume [Ws/mm ²]
1	0.0	4,000.0	0.000	0.000	28.0	2,000.0	0.014	0.350
2	0.0	4,000.0	0.000	0.000	35.0	2,000.0	0.018	0.438
3	0.0	4,000.0	0.000	0.000	42.0	2,000.0	0.021	0.525
4	0.0	4,000.0	0.000	0.000	35.0	1,666.7	0.021	0.525
5	0.0	4,000.0	0.000	0.000	35.0	2,000.0	0.018	0.438
6	0.0	4,000.0	0.000	0.000	35.0	2,500.0	0.014	0.350
7	110.4	390.0	0.283	7.077	64.0	0.008	0.080	2.000
8	124.2	390.0	0.318	7.962	72.0	0.008	0.090	2.250
9	138.0	390.0	0.354	8.846	80.0	0.008	0.100	2.500
10	151.8	390.0	0.389	9.731	88.0	0.008	0.110	2.750
11	165.6	390.0	0.425	10.615	96.0	0.008	0.120	3.000
12	138.0	487.5	0.283	7.077	80.0	1,000.0	0.080	2.000
13	138.0	433.3	0.318	7.962	80.0	888.9	0.090	2.250
14	138.0	390.0	0.354	8.846	80.0	0.008	0.100	2.500
15	138.0	354.5	0.389	9.731	80.0	727.3	0.110	2.750
16	138.0	325.0	0.425	10.615	80.0	666.7	0.120	3.000
Source: Table by authors								

Figure 3 (a) Photograph of a typical truncheon specimen (specimen 9), indicating up- and down-skin surfaces, and locations where we measure surface topography (maroon markers). An inset image shows a magnified optical image of typical as-built surface topography and (b) a typical WLI surface topography measurement z = f(x,y)



Source: Figure by authors

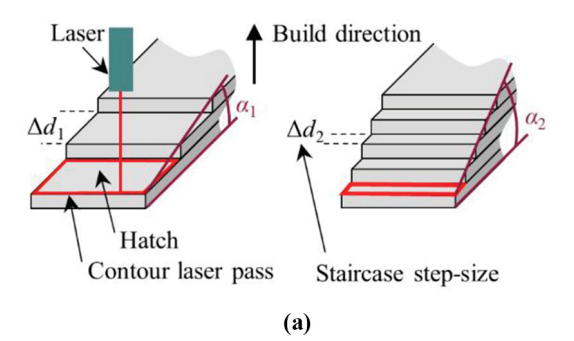
an inclination of $\alpha=5^{\circ}$ requires a distance of $\Delta d=474\,\mu\mathrm{m}$ between adjacent stairsteps, which is apparent in the surface topography as equidistant raised contour laser lines [red color in Figure 4(b)].

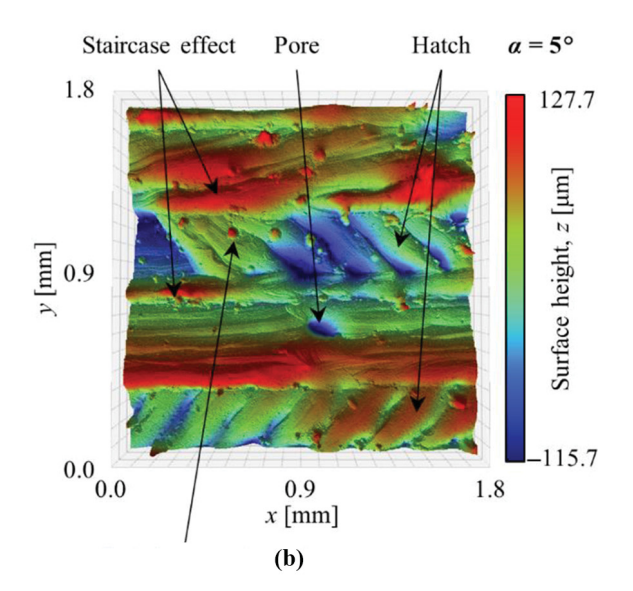
The area between stairsteps, which increases with decreasing build orientation α , reveals herringbone-shaped laser scan lines that result from the laser following a hatch pattern when printing the bulk of the layer (Reijonen *et al.*, 2020). We also observe pores in the as-built surface topography, which present as recess areas on the surface that result from incomplete fusion of the metal powder particles [dark blue color in Figure 4(b)] and negatively impact the mechanical properties of the part (du Plessis *et al.*, 2020; Kim and Moylan, 2018; Maleki *et al.*, 2021;

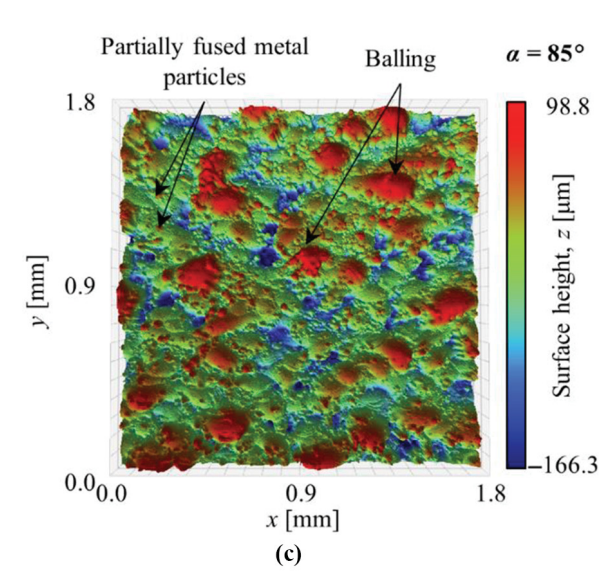
Al-Maharma *et al.*, 2020). In addition, the as-built surface topography shows partially fused metal powder particles that adhere to the as-built surface as a result of excessive heating (Li *et al.*, 2012) [small spherical raised structures, red in Figure 4(b) and (c)]. Finally, the onset of melt pool instability occurs under specific conditions in which the melt pool does not fully wet the previously sintered layer, which is referred to as "balling." Figure 4(c) shows a surface topography measurement of an as-built surface manufactured with a build orientation $\alpha = 85^{\circ}$, depicting features that result from balling [raised spherical structures, red in Figure 4(c)], which causes a rough surface finish and may create geometric inaccuracy (Li *et al.*, 2012).

Volume 31 · Number 1 · 2025 · 200-217

Figure 4 (a) Schematic of the LPBF process that manufactures oblique or curved surfaces by stacking layers like a staircase in the build direction, and surface topography maps that illustrate surface topography features characteristic of as-built LPBF surfaces; showing (b) staircase effect, laser scan lines/hatch pattern and pores (specimen 2, build orientation $\alpha=5^{\circ}$), and (c) partially fused metal particles and balling (specimen 2, build orientation $\alpha=85^{\circ}$)







Source: Figure by authors

We characterize the as-built surface topography using areal and deterministic surface topography parameters. Areal surface topography parameters include the surface roughness Sa, RMS surface roughness Sq, skewness Ssk and kurtosis Sku, as defined in ISO 25178-2 [ISO 25178-2:2021(En), 2021]. The skewness characterizes the distribution of peaks and valleys on the surface, with Ssk = 0 indicating an equal distribution of peaks and valleys, and Ssk > 0 and Ssk < 0 indicating more and fewer peaks than valleys, respectively. The kurtosis quantifies the sharpness of the surface topography, with Sku > 3indicating a surface with sharp peaks and Sku < 3 a surface with rounded peaks. Alternatively, deterministic surface topography parameters include asperity density η_s , mean asperity radius R_s and standard deviation of asperity heights σ_s . To determine the deterministic surface topography parameters, we first identify each peak i of the surface topography map using an eightnearest neighbor scheme (Pawar et al., 2012; Kalin et al., 2016; Mahboob Kanafi and Tuononen, 2017). The standard deviation of asperity heights σ_s derives directly from the peak heights, whereas the asperity density η_s results from the number of peaks and the nominal surface area of the surface topography measurement. The curvature of each peak i in two orthogonal directions x and y is $\kappa_{x,i} = d^2z/dx^2$ and $\kappa_{y,i} = d^2z/dy^2$, and the radius of curvature ρ_i of that peak is the inverse of the average of its κ_x and κ_y , i.e. $\rho_i = -\left[(\kappa_{x,i} + \kappa_{y,i})/2\right]^{-1}$. The mean asperity radius R_s is the arithmetic mean of all individual peak radii. We use a central finite difference scheme to calculate the derivatives of the surface heights dz/dx and d^2z/dx^2 .

We present the results as follows. First, we evaluate the effect of one versus two contour laser passes on the as-built surface topography (see Section 3.1). Second, we compare areal and deterministic surface topography parameters in the context of unambiguously characterizing as-built LPBF surface topography, and we discuss the limitations of areal surface topography parameters (see Section 3.2). Finally, we evaluate the effect of changing combinations of LPBF process parameters on the as-built surface topography (see Section 3.3).

3. Results and discussion

3.1 Effect of one and two contour laser passes on the asbuilt surface topography

Truncheon specimens 2 and 9 are representative of all specimens manufactured with one and two contour laser passes, respectively, based on qualitative and quantitative analysis of the as-built surface topography maps. Table 2 and 3 show 1.8 mm × 1.8 mm as-built surface topography maps of specimen 2 (one contour laser pass) and specimen 9 (two contour laser passes) to visually illustrate the effect of the build orientation $0^{\circ} \le \alpha \le 90^{\circ}$ on the as-built surface topography. In addition, Figure 5 shows the surface topography parameters that characterize the as-built surface topography maps as a function of the build orientation α , including areal surface topography parameters (a) Sa, (b) Ssk, and (c) Sku, and deterministic surface topography parameters (d) η_s , (e) R_s , and (f) σ_s for specimens 2 (orange, square marker) and 9 (maroon, round marker). Figure 5(f) also includes the roughness parameter σ_s/R_s for both specimens 2 and 9 (teal). Figure 5 includes the surface

Volume 31 · Number 1 · 2025 · 200–217

Table 2 As-built surface topography maps (1.8 mm \times 1.8 mm) and topography parameters for specimen 2 manufactured with one contour laser pass

α [°]	0	10	20	30	40
Surface topography map					
<i>Sp</i> [μm]	92.981	159.205	119.731	143.619	125.900
Sv [µm]	76.055	-128.834	-128.443	-109.090	-144.359
Sa [µm]	16.971	28.992	27.534	25.089	26.292
Ssk [-]	0.116	0.669	0.405	0.571	0.112
Sku [-]	2.990	3.922	2.990	3.341	3.239
$\eta_s [\mu m]$	0.095	0.068	0.065	0.079	0.072
R_s [µm]	1.102	0.845	0.787	0.502	0.493
σ_s [μ m]	21.509	34.072	34.097	31.065	32.957
σ_s/R_s [-]	19.518	40.322	43.325	61.882	66.850
α [°]	50	60	70	80	90
Surface topography map					
<i>Sp</i> [μm]	214.796	135.382	151.328	127.084	98.496
Sν [μm]	- 145.750	-115.921	- 127.748	-134.981	- 161.073
Sa [μm]	23.742	21.657	21.710	18.219	19.433
Ssk [-]	0.198	0.069	0.304	0.110	-0.175
Sku [-]	3.545	3.660	3.738	3.680	3.846
η_s [µm]	0.069	0.073	0.068	0.068	0.062
R_s [µm]	0.484	0.470	0.578	0.590	0.641
σ_s [μ m]	29.640	27.534	27.422	23.131	24.590
σ_s/R_s [-]	61.240	58.583	47.443	39.205	38.362

Source: Table by authors

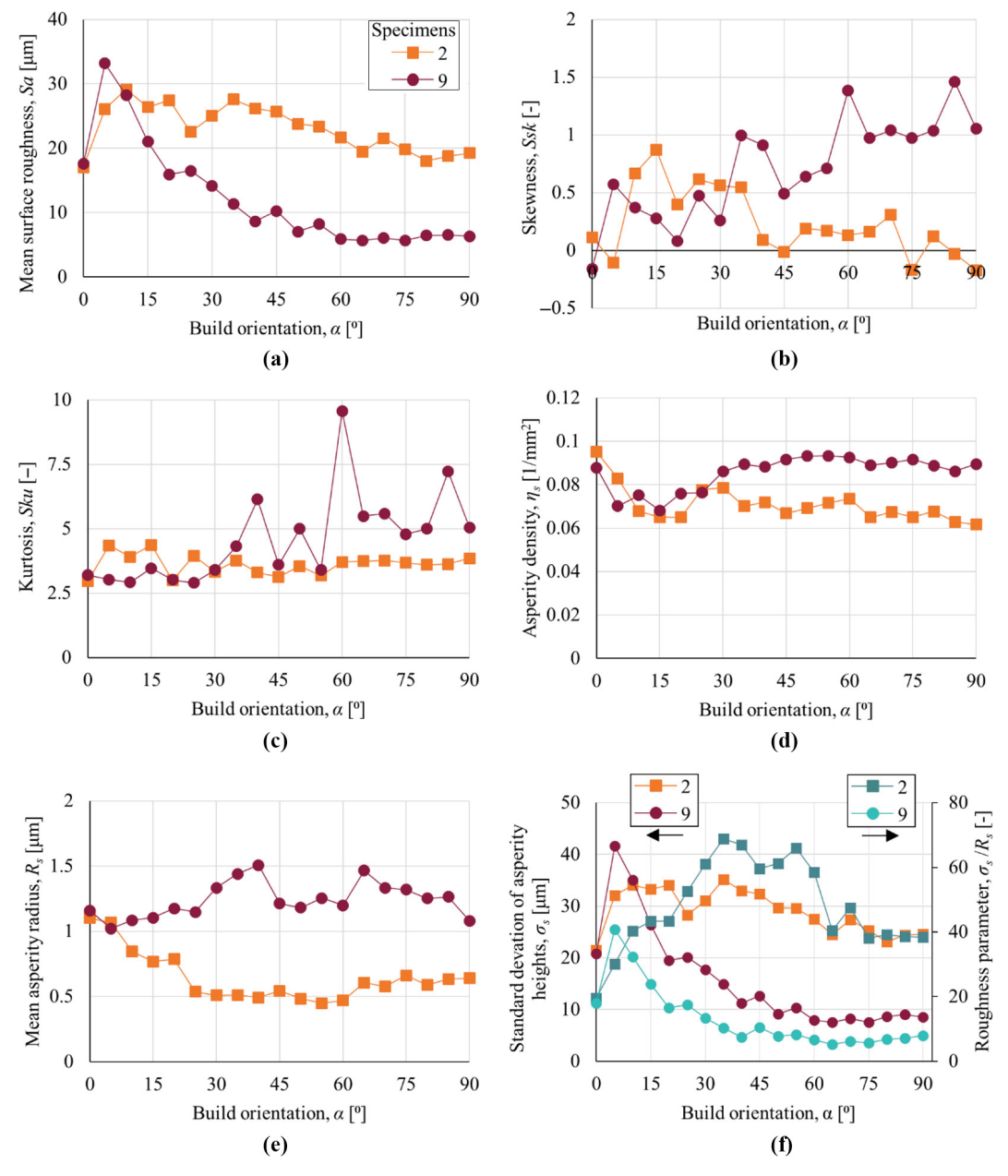
Table 3 As-built surface topography maps (1.8 mm \times 1.8 mm) and topography parameters for specimen 9 manufactured with two contour laser passes

α [°]	0	10	20	30	40
Surface topography map					
<i>Sp</i> [μm]	73.728	115.369	80.891	60.972	77.362
Sv [μm]	-98.401	-93.411	-92.375	-99.377	-44.648
Sa [µm]	17.554	28.212	15.922	14.119	8.660
Ssk [-]	-0.161	0.371	0.080	0.259	0.911
Sku [-]	3.202	2.919	3.016	3.399	6.137
η_s [µm]	0.088	0.075	0.076	0.086	0.088
R_s [µm]	1.157	1.085	1.175	1.335	1.508
σ_s [µm]	20.845	35.086	19.523	17.755	11.279
σ_s/R_s [-]	18.016	32.337	16.615	13.300	7.479
α [°]	50	60	70	80	90
Surface topography map					
<i>Sp</i> [μm]	66.945	81.203	68.473	61.355	49.098
Sv [µm]	-49.862	-36.520	-30.615	-35.545	-42.319
Sa [μm]	7.050	5.884	6.028	6.424	6.336
Ssk [-]	0.638	1.386	1.038	1.036	1.055
Sku [-]	4.995	9.574	5.585	5.001	5.052
η_s [μ m]	0.093	0.093	0.090	0.089	0.090
R_s [µm]	1.186	1.199	1.334	1.253	1.081
σ_s [μ m]	9.129	7.910	8.218	8.628	8.503
σ_s/R_s [-]	7.697	6.597	6.160	6.886	7.868

Source: Table by authors

Volume 31 · Number 1 · 2025 · 200-217

Figure 5 As-built surface topography parameters for specimen 2, manufactured with one laser contour pass (orange, square marker) and specimen 9, manufactured with two contour laser passes (maroon, round marker) as a function of build orientation; showing (a) mean surface roughness; (b) skewness; (c) kurtosis and (d) asperity density; (e) mean asperity radius and (f) standard deviation of asperity heights and roughness parameter σ_s/R_s



Source: Figure by authors

topography parameters for all build orientations α of the truncheon specimen, i.e. using $\alpha=5^\circ$ increments (19 surface topography measurements), whereas Tables 2 and 3 only show topography maps with $\alpha=10^\circ$ increments (10 surface topography measurements) for brevity. Note that the surface topography parameters of all 16 specimens are available in the Supplemental Information.

Qualitatively comparing the surface topography maps of Tables 2 and 3 shows similar surface topography features for both specimens 2 and 9 at each build orientation α . However, the as-built surface topography with two contour laser passes

(specimen 9) appears smoother than that with one contour laser pass (specimen 2). Correspondingly, the Sa and σ_s/R_s values are up to 73% and 89% lower for the surfaces with two compared to one contour laser pass because the former covers a larger surface area than the latter (see Figure 2), which reduces the surface roughness, similar to e.g. laser polishing processes (Raeymaekers and Talke, 2010).

Specifically, we observe from Tables 2 and 3 that laser scan lines dominate the surface topography when $\alpha = 0^{\circ}$ because the interior hatching pattern covers the entire flat top surface of the specimen. However, the LPBF process approximates an

Volume 31 · Number 1 · 2025 · 200–217

inclined top surface by stacking multiple staggered layers that form stairsteps [so-called "staircase" effect; see schematic in Figure 4(a)]. Since the contour laser pass only traces the perimeter of each of those staggered layers, we observe parallelspaced contour laser scan lines that correspond to the stairsteps to approximate the inclination of the surface. The staircase effect is particularly pronounced for shallow build orientations $\alpha < 15^{\circ}$, where the distance between adjacent stairsteps is largest and the laser contour passes do not cover the entire surface area between stairsteps. As a result, we discern the interior hatch pattern that forms the bulk of the specimen in between the contour laser scan lines. This hatch pattern is less apparent on the as-built surfaces of specimen 9 than on those of specimen 2 because two compared to one contour laser pass cover a larger surface area. Increasing the build orientation $\alpha > 15^{\circ}$ decreases the distance between stairsteps that approximate the surface inclination. Hence, the contour laser pass covers almost the entire interior hatch pattern and reduces the presence of the interior hatch pattern in the as-built surface topography. However, increasing areas of balling occur, i.e. de-wetting of the melt pool when the build orientation $\alpha > 50^{\circ}$, because the distance between contour laser passes decreases, which in turn increases the temperature of the laser melt pool (Jia and Gu, 2014). Balling is less distinct on the as-built surfaces of specimen 9 than on those of specimen 2, which suggests that the second contour laser pass smoothens balling artifacts on the surface caused by the first contour laser pass.

In addition, the surface topography maps of Tables 2 and 3 show partially fused metal powder particles on the as-built surfaces, which attach at the edge of the melt pool of the contour laser pass where the temperature is not sufficiently high to fully fuse them. The number of partially fused metal particles increases with increasing build orientation α because the distance between the contour passes in adjacent layers decreases, thus increasing the number of locations where metal particles partially fuse to the surface. Similarly, the number of partially fused metal particles increases with increasing number of contour laser passes because the contour laser passes only overlap partially, thus creating multiple regions where the melt pool temperature causes partial fusion of particles.

Table 2 does not show a trend in the maximum peak height Sp and valley depth Sv as a function of the build orientation α for specimen 2. When $\alpha \leq 15^\circ$, Sp and Sv depend on the contour laser lines and interior hatch pattern features, whereas when $\alpha \geq 50^\circ$ they depend on instances of balling. In contrast, Table 3 shows a marked decrease of Sp and Sv with increasing build orientation for specimen 9, when $\alpha \geq 40^\circ$. Two contour laser passes in combination with small stairsteps result in smooth as-built surfaces, and Sp and Sv depend on the presence of partially fused metal powder particles.

From Figure 5, we observe that when $\alpha=0^\circ$, the different surface topography parameters are almost identical for specimens 2 and 9, which matches the qualitative observations of the surface topography maps depicted in Tables 2 and 3. The interior hatch laser parameters, which are consistent across all specimens, drive the as-built surface topography of the majority of the exposed top surface because the contour laser pass(es) only cover the perimeter of the specimen. However, when $\alpha \neq 0^\circ$ specimens 2 and 9 show different surface topography parameters. Specifically, Figure 5(a) shows that Sa increases

with increasing build orientation when the staircase effect dominates the surface topography for shallow build orientations ($0^{\circ} \le \alpha \le 10^{\circ}$). Yet, Sa decreases with increasing build orientation when the importance of the staircase effect decreases ($\alpha > 10^{\circ}$). The use of two compared to one contour laser pass results in a lower Sa for specimen 9 than for specimen 2, which is also qualitatively apparent in Tables 2 and 3.

Figure 5(b) shows that the skewness Ssk slightly decreases (specimen 2) and increases (specimen 9) with increasing build orientation α . Similarly, Figure 5(c) shows that the kurtosis Sku remains constant (specimen 2) and increases (specimen 9) with increasing α . Table 2 illustrates that the surface topography of specimen 2 remains almost unchanged when $\alpha > 40^{\circ}$, which explains its almost constant Ssk, Sku, and Sa [Figure 5(a)]. $Ssk \approx 0$ signifies an approximately equal distribution of peaks and valleys, and Sku = 3 indicates rounded surface topography features, which suggests balling or the interior hatch pattern. The combination of $Ssk \approx 0$ and Sku = 3 indicates that the distribution of surface heights shows characteristics of a normal distribution.

In contrast, Table 3 illustrates that the surface topography of specimen 9 smoothens with increasing build orientation ($\alpha > 10^{\circ}$), evidenced by decreasing Sa. Hence, the partially fused metal powder particles, which are increasingly present with increasing α , dominate the surface topography of an increasingly smooth surface. Consequently, the as-built surface topography is positively skewed Ssk > 0, i.e. it shows a larger number of peaks than valleys, and shows a kurtosis Sku > 3, reflecting the sharpness (or "spikiness") of the as-built surface dominated by partially fused metal powder particles.

The deterministic surface topography parameters, i.e. the asperity density η_s [Figure 5(d)], mean asperity radius R_s [Figure 5(e)], and standard deviation of asperity heights σ_s [Figure 5(f)], support the observations and physical explanation of the areal surface topography parameter results. Specifically, Figure 5(d) shows that η_s increases with increasing α for specimen 9, but remains approximately constant for specimen 2 when $\alpha > 30^{\circ}$, i.e. when the staircase effect is not the primary driver of the as-built surface topography. Since the asperity density captures the number of local peaks on the as-built surface, it is primarily driven by the number of partially fused metal powder particles (which show as small local peaks), which increase with increasing α for specimen 9. They are not the dominant surface topography feature for specimen 2, where large balling features dominate the topography. Similarly, the mean asperity radius R_s is a measure of the smoothness of the surface, where smoothness increases with increasing R_s . We observe that the mean asperity radius R_s is larger for specimen 9 than for specimen 2, which is in agreement with the Sa parameter. The standard deviation of asperity heights σ_s decreases with increasing build orientation α for specimen 9, but remains approximately constant (or decreases slightly) for specimen 2 when $\alpha > 15^{\circ}$, i.e. when the staircase effect is not the dominant determinant of the surface topography. The ratio of σ_s and R_s expresses the roughness of the surface [teal color in Figure 5(f)], thus clearly indicating that the roughness of specimen 9 is lower than that of specimen 2, which is in agreement with the areal surface topography parameters.

Volume 31 · Number 1 · 2025 · 200-217

3.2 Limitations of areal versus deterministic surface topography parameters

Most studies use areal surface topography parameters to characterize the as-built surface topography of LPBF parts, likely because these parameters are well-known, are defined in standards [ISO 25178-2:2021(En), 2021] and are easily extracted from optical profilometry measurements using commercial software. However, the interpretative value of areal surface topography parameters is questionable because visibly different surfaces sometimes show similar areal surface topography parameters or, conversely, similar areal surface topography parameters hide vastly different surface topography (Mate and Carpick, 2019). This is because areal surface topography parameters average surface heights over the entire measurement area, e.g. Sa, Sq, or are based on a single measurement point with reference to the center plane, e.g. Sv, Sp. We illustrate this problem for two selected surface topography maps, which are typical for the entire data set.

Table 4 shows a side-by-side comparison of as-built surface topography maps of truncheon specimens 10 and 12, with their respective areal and deterministic surface topography parameters. We qualitatively observe that both specimens show a substantially different surface topography since they were manufactured with different LPBF process parameters, including laser scan speed and power (see Table 1), and build orientation. Specifically, specimen 10 was manufactured using a build orientation $\alpha = 50^{\circ}$ and displays instances of balling, whereas specimen 12 was manufactured with $\alpha = 0^{\circ}$ and shows the interior hatch pattern. Despite the substantially different surface topography maps, Table 4 shows that the areal surface topography parameters Sa, Sq, and Ssk are almost identical for both specimens and display a difference of less than 4%. In contrast, the deterministic surface topography parameters show

Table 4 Comparison between areal and deterministic surface topography parameters

Specimen #	10	12				
α [°]	50	0				
Surface topography						
Surface top	Surface topography parameter values (difference [%])					
Sa [µm]	12.01	12.43 (3.5)				
Sq [µm]	15.83	16.41 (3.63)				
Ssk [-]	0.75	0.75 (0.13)				
Sku [-]	4.38	5.68 (29.79)				
$\eta_s [1/\text{mm}^2]$	950.75	877.59 (7.69)				
σ_s [μ m]	6.50	7.76 (19.34)				
R_s [µm]	3.88	3.61 (6.91)				
$\sigma_{_{S}}/R_{S}$	1.68	2.15 (27.98)				

Source: Table by authors

much more significant differences between both surfaces, which range between 6.91% for R_s and 19.34% for σ_s and, thus, capture the qualitatively different surface topography maps. However, we note that the kurtosis Sku shows a difference of 29.79% between both surface topography maps and, in this particular comparison, suggests that both surface topography maps are different. The ratio of the standard deviation of asperity heights and mean asperity radius σ_s/R_s is a measure for the surface roughness. Specimen 10 and 12 show $\sigma_s/R_s = 1.68$ and $\sigma_s/R_s = 2.15$, i.e. a 28% difference, which reflects the difference in their surface topography, depicted in Table 4. Yet, the average surface roughness Sa shows just a 3.5% difference between both surfaces, despite their surface topography qualitatively appearing substantially different. Thus, the large percent difference between the σ_s/R_s and Sa values for Specimen 10 and 12 emphasizes the importance of either considering several areal surface topography parameters instead of only relying on Sa (e.g. using Sv, Sp, Ssk, and Sku), or using deterministic surface topography parameters to characterize the as-built surface topography. We note that deterministic surface topography parameters also show limitations since they rely on identifying local peaks, e.g. using four or eight nearest neighbors, and the numerical discretization of the mathematical derivatives to calculate the peak curvatures (Kalin et al., 2016).

3.3 Effect of laser powder bed fusion process parameters on the as-built surface topography

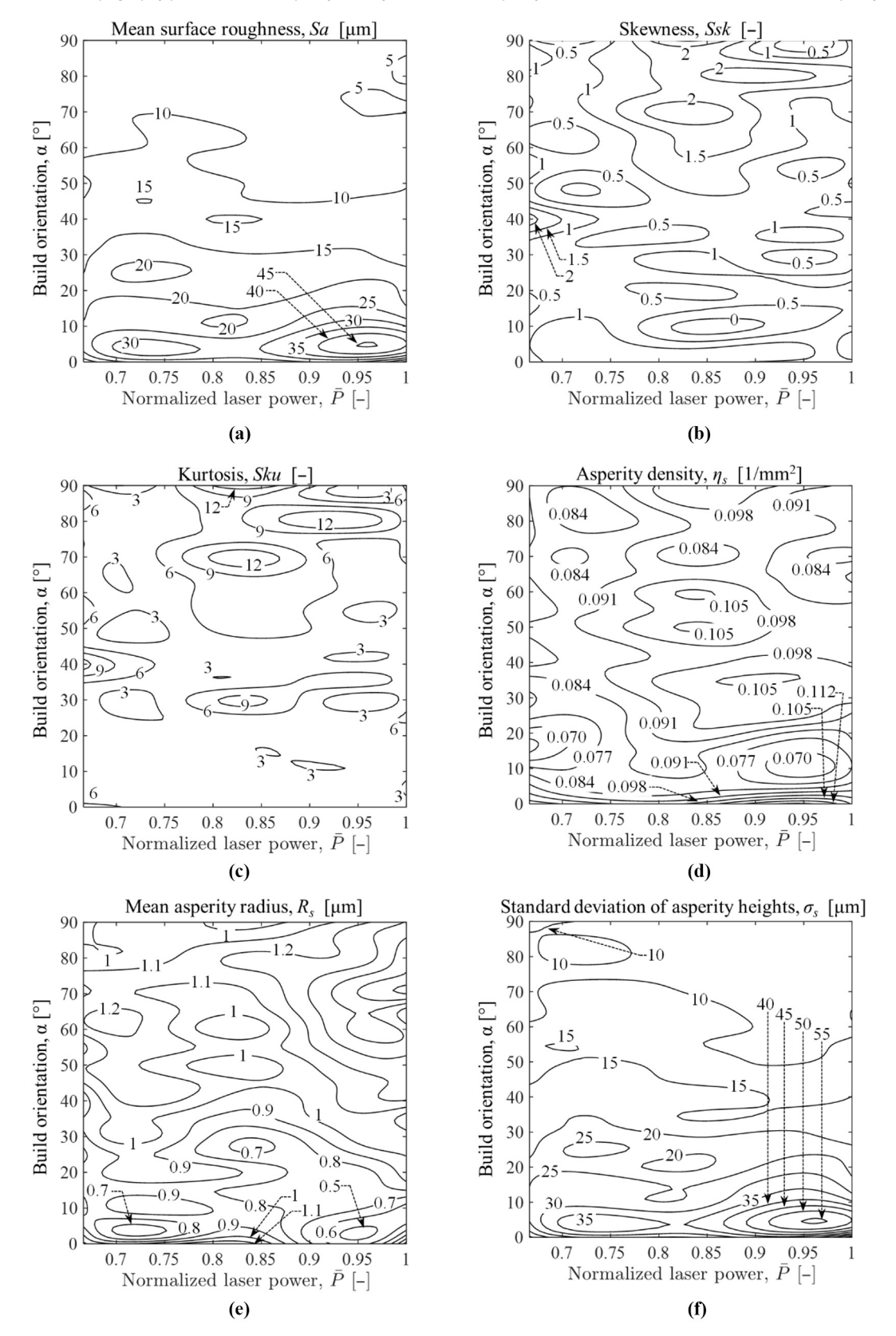
We compare the individual and combined effects of contour laser power, scan speed and build orientation on the as-built surface topography. We specifically select truncheon specimens 7 through 16, which are manufactured using two contour laser passes (see Table 1), with parameters optimized for up-skin surfaces. We define the normalized laser power $\overline{P} = P/P_{\text{max}}$, with P_{max} the maximum laser power, and the normalized laser scan speed $\overline{V} = V/V_{\text{max}}$, with V_{max} the maximum laser scan speed. We methodically vary the laser power with constant laser scan speed (specimens 7–11), and vary laser scan speed with constant laser power (specimens 12–16).

Figure 6 shows the areal surface topography parameters (a) Sa, (b) Ssk, and (c) Sku, and deterministic surface topography parameters (d) η_s , (e) R_s , and (f) σ_s as a function of build orientation α and normalized laser power \overline{P} , for constant normalized laser scan speed $\overline{V}=0.80$. From Figure 6(a), we observe that the mean surface roughness Sa decreases with increasing build orientation α , and that $\alpha \leq 15^\circ$ results in substantially higher Sa than $\alpha > 15^\circ$ because the staircase effect dominates the surface topography (except when $\alpha = 0^\circ$, when the staircase effect does not occur). Furthermore, when $\alpha \leq 15^\circ$, Sa increases slightly with increasing normalized laser power \overline{P} .

From Figure 6(b), we observe that the skewness Ssk appears almost independent of the contour laser power \overline{P} but increases with increasing build orientation α . When $\alpha > 50^{\circ}$, partially fused metal powder particles dominate the surface topography, which increases the number of peaks relative to the number of valleys, and, thus, Ssk increases. Similarly, Figure 6(c) shows that the kurtosis Sku increases with increasing α and with increasing contour laser power \overline{P} . This observation is in agreement with the results of Table 3, which show that the number of partially fused metal powder particles increases with

Volume 31 · Number 1 · 2025 · 200–217

Figure 6 Relationship between as-built surface topography parameters, the build orientation and the normalized contour laser power for constant normalized laser scan speed \overline{V} = 0.80, showing areal surface topography parameters (a) mean surface roughness Sa, (b) skewness Ssk, (c) kurtosis Sku, and deterministic surface topography parameters (d) asperity density η_s , (e) mean asperity radius R_s , and (f) standard deviation of asperity heights σ_s



Source: Figure by authors

Volume 31 · Number 1 · 2025 · 200–217

increasing α , thus increasing the sharpness of the surface topography. In addition, increasing \overline{P} also increases the number of partially fused metal powder particles because the temperature of the melt pool increases, thus potentially fusing additional metal powder particles to the as-built surfaces.

From Figure 6(d) we observe no clear trend between the build orientation α , the contour laser power \overline{P} and the asperity density η_s , even though η_s appears to increase slightly with increasing \overline{P} , driven by an increasing number of partially fused metal powder particles. Figure 6(e) shows that the mean asperity radius R_s increases with increasing build orientation α and with increasing contour laser power \overline{P} because increasing \overline{P} widens the melt pool and smoothens the surface topography. In addition, from Figure 6(f) we observe that the standard deviation of asperity heights σ_s decreases with increasing build orientation α but increases with increasing contour laser power \overline{P} when $\alpha \leq 15^{\circ}$ and is independent of \overline{P} when $\alpha > 15^{\circ}$. Thus, the results of σ_s are similar to those of Sa, which is expected because they both derive from the variation of surface heights. The combination of Figure 6(e) and (f), shows that the surface roughness, i.e. σ_s/R_s decreases with increasing α and decreases with decreasing \overline{P} for $\alpha < 15^{\circ}$, yet decreases with increasing \overline{P} for $\alpha > 15^{\circ}$.

Figure 7 shows the areal surface topography parameters (a) Sa, (b) Ssk, and (c) Sku, and deterministic surface topography parameters (d) η_s , (e) R_s , and (f) σ_s as a function of build orientation α and normalized laser scan speed \overline{V} , for constant normalized laser power $\overline{P} = 1.00$. (note that Figure 6 shows the surface topography results for constant \overline{V}). From Figure 7(a), we observe that the mean surface roughness Sa decreases with increasing build orientation α , and that $\alpha < 15^{\circ}$ results in substantially higher Sa than $\alpha > 15^{\circ}$ because the staircase effect dominates the surface topography (except when $\alpha = 0^{\circ}$, when the staircase effect does not occur). Furthermore, when $\alpha < 15^{\circ}$, Sa first increases and then decreases with increasing \overline{V} because two competing effects are at play. Increasing \overline{V} reduces the temperature of the melt pool, which reduces smoothing of the surface topography and increases surface roughness. However, increasing \overline{V} also increases the relative importance of the surface roughness of the interior hatch pattern compared to the contour laser lines (for $\alpha \leq 15^{\circ}$) because the width of the melt pool decreases, which reduces the surface roughness. As a result, the maximum Sa value occurs in the middle of the range of the normalized scan speeds we evaluate.

From Figure 7(b), we observe that skewness Ssk appears almost independent of the laser scan speed \overline{V} but increases with increasing build orientation α . When $\alpha > 50^{\circ}$, partially fused metal powder particles dominate the surface topography, which increases the number of peaks relative to the number of valleys and, thus, increases Ssk. Figure 7(c) shows that the kurtosis Sku increases with increasing build orientation α and increasing contour laser scan speed \overline{V} , which is in agreement with the results of Table 3, which show that the number of partially fused metal powder particles increases with increasing α , thus increasing the sharpness of the surface topography. From Figure 7(d), we observe no clear trend between the build orientation α , the contour laser scan speed \overline{V} and the asperity density η_s , even though η_s appears to increase slightly with increasing \overline{V} . Figure 7(e) shows that the mean asperity radius R_s is almost independent of the build orientation α and the laser scan speed \overline{V} . In addition, from Figure 7(f), we observe that the standard deviation of asperity heights σ_s decreases with increasing α , but first increases and then decreases with increasing \overline{V} when $\alpha \leq 15^{\circ}$. Thus, the results of σ_s are similar to those of Sa, which is expected because they both derive from the variation of surface heights. Combining Figure 7(e) and (f), shows that the roughness parameter, i.e. σ_s/R_s , decreases with increasing α and first decreases and then increases with decreasing \overline{V} when $\alpha \leq 15^{\circ}$, yet is independent of \overline{V} when $\alpha > 15^{\circ}$.

Finally, when comparing the gradients of the contours in Figures 6 and 7, we observe that the surface topography parameters are less sensitive to the contour laser scan speed than to the contour laser power.

3.4 Modifying laser powder bed fusion process parameters while maintaining constant energy density

Previous work suggests that the laser energy density is the primary parameter that determines the as-built surface topography of LPBF specimens (Watring et al., 2019; Detwiler et al., 2022; Boswell et al., 2021; Elambasseril et al., 2022). However, we show that for shallow build orientations α , the relative magnitude of contour laser power \overline{P} and contour laser scan speed \overline{V} , which define the laser energy density, also play a role.

Figure 8 shows as-built surface topography maps of truncheon specimens 11 (\overline{V} = 0.800) (maroon, circle markers) and 16 (\overline{V} = 0.667) (orange, square markers), which are manufactured with identical laser energy density for both laser contour passes (Contour 1 and Contour 2), vet different relative combinations of \overline{P} and \overline{V} , for four build orientations $\alpha = 0^{\circ}$, 10° , 60° and 90° . The average surface roughness Sa and the roughness parameter σ_s/R_s are different between both specimens for $5^{\circ} \le \alpha \le 15^{\circ}$. Correspondingly, the surface topography maps for $\alpha = 10^{\circ}$ show that different combinations of \overline{P} and \overline{V} , even while maintaining constant energy density, result in substantially different surface topography. Specifically, decreasing \overline{V} increases balling, which is in agreement with results documented by Li et al. (Townsend et al., 2016). Furthermore, when $\alpha > 30^{\circ}$ the distance between stairsteps is small and the contour laser passes cover the entire as-built surface, thereby reducing the surface roughness compared to $\alpha < 30^{\circ}$. Consequently, almost no difference exists between Sa and σ_s/R_s for specimens 11 and 16 when $\alpha > 30^\circ$.

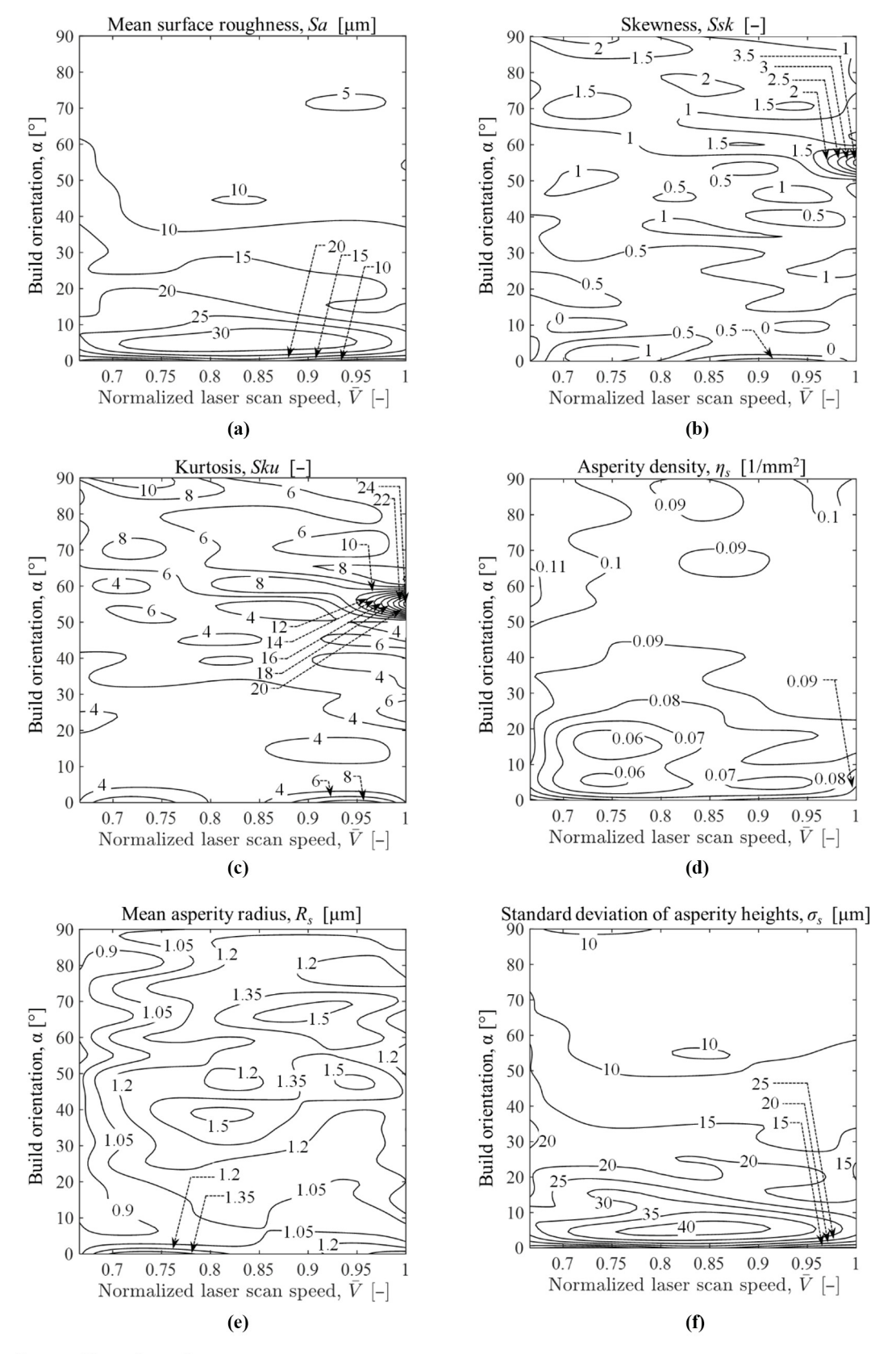
3.5 Limitations

Our experimental work also shows limitations. First, the optical profilometry surface topography measurement shows limited spatial and vertical resolution. In addition, the resolution must be balanced with the field-of-view. We performed a convergence study (see Section 2.2) to select the measurement parameters that render the results of the surface topography measurements independent of the measurement parameters.

The reflectivity of the surfaces also plays an important role in the quality of the optical profilometry measurement. The coarse as-built IN718 LPBF surfaces display poor reflectivity (see Figure 3), which causes light scattering and causes difficulty to obtain high-quality surface topography measurements. A data reconstruction algorithm, included in the Bruker Vision 64

Volume 31 · Number 1 · 2025 · 200–217

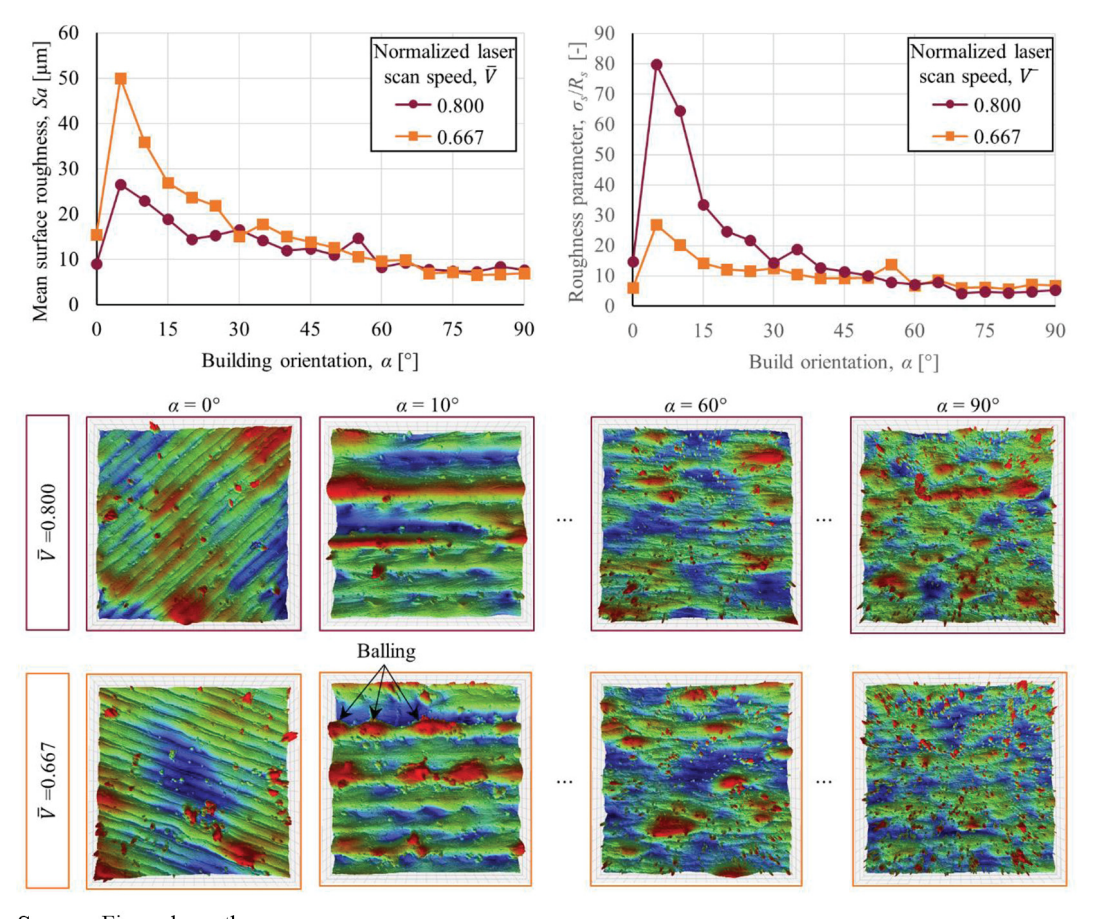
Figure 7 Relationship between as-built surface topography parameters, the build orientation and the normalized contour laser scan speed for constant normalized laser power $\overline{P}=1.00$, showing areal surface topography parameters (a) mean surface roughness Sa; (b) skewness Ssk; (c) kurtosis Sku, and deterministic surface topography parameters (d) asperity density η_s ; (e) mean asperity radius R_s and (f) standard deviation of asperity heights σ_s



Source: Figure by authors

Volume 31 · Number 1 · 2025 · 200–217

Figure 8 As-built surface topography maps and selected surface topography parameters of truncheon specimens 11 ($\overline{V} = 0.800$) and 16 ($\overline{V} = 0.667$), which are manufactured with identical laser energy density for both laser contour passes (Contour 1 and 2), yet different relative combinations of laser power and laser scan speed, as a function of the build orientation α



Source: Figure by authors

software and based on a Gaussian filter, may fill-in 5% of potentially missing data points.

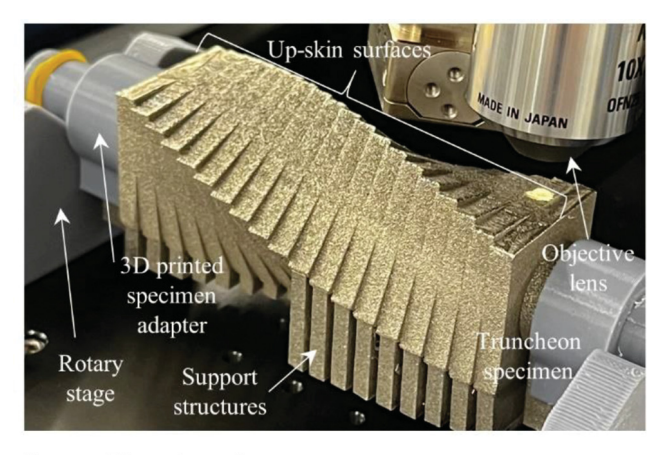
The convergence study informs the need for a 3 x 3 array of optical surface topography measurements to combine the required spatial resolution with the field-of-view needed to capture the distinct features characteristic of as-built LPBF surface topography. However, stitching together multiple surface topography maps to obtain the required field-of-view is time-consuming, in particular in light of the large number of truncheon specimens (16) and as built surfaces (19 per truncheon). To reduce the experimental burden, researchers could consider supplementing experimental surface topography measurements with synthetic surface topography data that is statistically similar to the experimental data and could add diversity to the overall data set. Methodologies to reliably create synthetic surface topography data of as-built LPBF surfaces have been documented in the literature [see, e.g. Senthilnathan et al. (2023); Seo et al. (2023)]. However, we did not include such data augmentation in this work.

To improve the practicality of performing surface topography measurements on the truncheon specimens, we devise a rotary stage that mounts the truncheon specimen and orients each of the as-built surfaces nominally flat with respect to the objective lens of the optical profilometer. Figure 9 illustrates a truncheon specimen mounted on the rotary stage by means of 3D printed adapters and depicts the position of the up-skin surfaces relative to objective lens of the optical profilometer. It also shows the support structures, attached to the down-skin surfaces, required to manufacture the truncheon specimen. The rotary stage ensures consistent fixturing, which helps create repeatable measurements and results.

Finally, manufacturing truncheon specimens with LPBF is time-consuming and costly. The truncheon specimens we use in this work required two separate build plates, which each required 40 h to complete. We only evaluate the up-skin surfaces because it was not possible to remove the support structures without altering the as-built down-skin surfaces (see Figure 9). Here, we focus on evaluating the combined effects of contour laser pass (one/two, laser power, laser scan speed) and build orientation on the as-built surface topography, considering both areal and deterministic surface topography parameters. We maintained all other LPBF process parameters constant. However, they might also affect the as-built surface topography. For instance, informed by the results documented in this work, it is possible that the layer thickness and definition of the hatch pattern could also affect the as-built surface

Volume 31 · Number 1 · 2025 · 200-217

Figure 9 Rotary stage to ensure consistent positioning of the up-skin as-built surfaces of the truncheon specimens relative to the objective lens of the white light interferometer



Source: Figure by authors

topography, in particular for shallow build orientations. However, we did not measure it, as this would require a new set of truncheon specimens.

4. Conclusions

A fundamental understanding of the relationship between LPBF process parameters and the as-built surface topography could enable manufacturing parts with tailored surface topography and thereby reduce or even eliminate the need for post-processing.

A methodical parameter study shows that the staircase effect dominates the as-built surface topography of surfaces manufactured with shallow build orientation ($\alpha < 15^{\circ}$). Balling and partially fused metal powder particles drive the as-built surface topography of surfaces manufactured with steep build orientations ($\alpha > 50^{\circ}$), for which the laser contour pass(es) cover the entire interior hatch pattern. Hence, the surface topography of as-built surfaces with a steep build orientation ($\alpha > 50^{\circ}$) is smoother than that of those with a shallow build orientation because the stairstep size decreases with increasing build orientation and, consequently, the contour laser pass covers an increasing section of the area between stairsteps, thus smoothing the as-built surface topography. Similarly, two compared to one contour laser pass cover a larger surface area, thus smoothing the as-built surface topography by covering the interior hatch pattern and eliminating other features such as balling.

We demonstrate for selected as-built surfaces manufactured with different LPBF process parameters that deterministic surface topography parameters quantify the distinct characteristics of as-built surface topography maps of qualitatively different topographies and, therefore, are more suitable to establish linkages with the LPBF process parameters than areal surface topography parameters.

We determine that simultaneously adjusting the laser power and laser scan speed have a combined effect on the as-built surface topography, even when maintaining constant laser energy density. However, the surface topography is less sensitive to changing the contour laser scan speed than the contour laser power.

These results provide guidelines for selecting LPBF process parameters that help achieve tailored, as-built surface topography without the need for post-processing. To that end, maximizing the smoothness (minimizing roughness) of as-built surfaces requires selecting a steep build orientation ($\alpha > 50^{\circ}$) or using a $\alpha = 0^{\circ}$ build orientation (top surface). Not only does selecting a steep build orientation minimize the staircase effect on the as-built surface topography, it also minimizes the sensitivity of the as-built surface topography to the contour laser power and laser scan speed, thus providing repeatability and consistency.

Acknowledgments

The authors thank Dr Junhyeon Seo for diligently measuring the as-built surface topography of all truncheon specimens and recording the surface topography parameters. BR acknowledges support from the Department of Defense, Office of Local Defense Community Cooperation award ST1605-21-04, and the National Science Foundation award CNS-2328112. TB acknowledges support of the KY-NASA award RIDG 23-07 and National Science Foundation award MRI-2216352. The authors also acknowledge the services of the Additive Manufacturing Institute of Science and Technology (AMIST) at the University of Louisville for fabrication of all truncheon specimens.

Supplementary material

The supplementary material for this article can be found online.

References

Al-Maharma, A.Y., Patil, S.P. and Markert, B. (2020), "Effects of porosity on the mechanical properties of additively manufactured components: a critical review", *Materials Research Express*, Vol. 7 No. 12, p. 122001.

Artzt, K., Mishurova, T., Bauer, P.-P., Gussone, J., Barriobero-Vila, P., Evsevleev, S., Bruno, G., Requena, G. and Haubrich, J. (2020), "Pandora's box-influence of contour parameters on roughness and subsurface residual stresses in laser powder bed fusion of Ti-6Al-4V", *Materials*, Vol. 13 No. 15, p. 3348.

Blakey-Milner, B., Gradl, P., Snedden, G., Brooks, M., Pitot, J., Lopez, E., Leary, M., Berto, F. and Du Plessis, A. (2021), "Metal additive manufacturing in aerospace: a review", *Materials & Design*, Vol. 209, p. 110008.

Boswell, J., Jones, J., Barnard, N., Clark, D., Whittaker, M. and Lancaster, R. (2021), "The effects of energy density and heat treatment on the microstructure and mechanical properties of laser additive manufactured Haynes 282", *Materials & Design*, Vol. 205, p. 109725.

Bourell, D., Kruth, J.P., Leu, M., Levy, G., Rosen, D., Beese, A.M. and Clare, A. (2017), "Materials for additive manufacturing", *CIRP Annals*, Vol. 66 No. 2, pp. 659-681.

Brown, C.U., Jacob, G., Possolo, A.M., Beauchamp, C.R., Peltz, M.A., Stoudt, M.R. and Donmez, M.A. (2018), "The

 $Volume~31 \cdot Number~1 \cdot 2025 \cdot 200-217$

- effects of laser powder bed fusion process parameters on material hardness and density for nickel alloy 625", NIST.
- Cabanettes, F., Joubert, A., Chardon, G., Dumas, V., Rech, J., Grosjean, C. and Dimkovski, Z. (2018), "Topography of as built surfaces generated in metal additive manufacturing: a multi scale analysis from form to roughness", *Precision Engineering*, Vol. 52, pp. 249-265.
- Calignano, F., Manfredi, D., Ambrosio, E.P., Iuliano, L. and Fino, P. (2013), "Influence of process parameters on surface roughness of aluminum parts produced by DMLS", *The International Journal of Advanced Manufacturing Technology*, Vol. 67 Nos 9/12, pp. 2743-2751.
- Cao, L., Li, J., Hu, J., Liu, H., Wu, Y. and Zhou, Q. (2021), "Optimization of surface roughness and dimensional accuracy in LPBF additive manufacturing", *Optics & Laser Technology*, Vol. 142, p. 107246.
- Carter, L.N., Villapún, V.M., Grover, L. and Cox, S.C. (2022), "Exploring the duality of powder adhesion and underlying surface roughness in laser powder bed fusion processed Ti-6Al-4V", Journal of Manufacturing Processes, Vol. 81, pp. 14-26.
- Detwiler, S. and Raeymaekers, B. (2022), "Deriving data-driven models that relate deterministic surface topography parameters of as-built Inconel 718 surfaces to laser powder bed fusion process parameters", Journal of Tribology, Vol. 144 No. 12, p. 121703.
- Detwiler, S., Watring, D., Spear, A. and Raeymaekers, B. (2022), "Relating the surface topography of as-built Inconel 718 surfaces to laser powder bed fusion process parameters using multivariate regression analysis", *Precision Engineering*, Vol. 74, pp. 303-315.
- Du Plessis, A. and Rossouw, P. (2015), "Investigation of porosity changes in cast Ti6Al4V rods after hot isostatic pressing", *Journal of Materials Engineering and Performance*, Vol. 24 No. 8, pp. 3137-3141.
- Du Plessis, A., Yadroitsava, I. and Yadroitsev, I. (2020), "Effects of defects on mechanical properties in metal additive manufacturing: a review focusing on X-ray tomography insights", *Materials & Design*, Vol. 187, p. 108385.
- Elambasseril, J., Rogers, J., Wallbrink, C., Munk, D., Leary, M. and Qian, M. (2022), "Laser powder bed fusion additive manufacturing (LPBF-AM): the influence of design features and LPBF variables on surface topography and effect on fatigue properties", pp. 1-37.
- Essa, K., Jamshidi, P., Zou, J., Attallah, M.M. and Hassanin, H. (2018), "Porosity control in 316L stainless steel using cold and hot isostatic pressing", *Materials & Design*, Vol. 138, pp. 21-29.
- Gibson, I., Rosen, D. and Stucker, B. (2014), Additive Manufacturing Technologies: 3D Printing, Rapid Prototyping, and Direct Digital Manufacturing, Springer New York, NY.
- Gockel, J., Sheridan, L., Koerper, B. and Whip, B. (2019), "The influence of additive manufacturing processing parameters on surface roughness and fatigue life", *International Journal of Fatigue*, Vol. 124, pp. 380-388.
- Huynh, T., Mehta, A., Graydon, K., Woo, J., Park, S., Hyer,
 H., Zhou, L., Imholte, D.D., Woolstenhulme, N.E., Wachs,
 D.M. and Sohn, Y. (2022), "Microstructural development
 in Inconel 718 Nickel-based superalloy additively

- manufactured by laser powder bed fusion", *Metallography*, *Microstructure*, and *Analysis*, Vol. 11 No. 1, pp. 88-107.
- ISO 25178-2:2021(En) (2021), "Geometrical product specifications (GPS) surface texture: areal part 2: terms, definitions and surface texture parameters".
- Jia, Q. and Gu, D. (2014), "Selective laser melting additive manufacturing of Inconel 718 superalloy parts: densification, microstructure and properties", *Journal of Alloys and Compounds*, Vol. 585, pp. 713-721.
- Jiang, R., Mostafaei, A., Pauza, J., Kantzos, C. and Rollett, A. D. (2019), "Varied heat treatments and properties of laser powder bed printed Inconel 718", Materials Science and Engineering: A, Vol. 755, pp. 170-180.
- Joe, J., Barber, J.R. and Raeymaekers, B. (2022), "A general load–displacement relationship between random rough surfaces in elastic, non-adhesive contact, with application in metal additive manufacturing", *Tribology Letters*, Vol. 70 No. 3, p. 77.
- Kafka, O.L., Benzing, J., Derimow, N., Schumacher, P., Koepke, L., Beamer, C., Godfrey, D. and Hrabe, N. (2023), "Effects of as-built surface with varying number of contour passes on high-cycle fatigue behavior of additively manufactured nickel alloy 718", *International Journal of Fatigue*, Vol. 176, p. 107872.
- Kalin, M., Pogačnik, A., Etsion, I. and Raeymaekers, B. (2016), "Comparing surface topography parameters of rough surfaces obtained with spectral moments and deterministic methods", *Tribology International*, Vol. 93, pp. 137-141.
- Karimialavijeh, H., Ghasri-Khouzani, M., Das, A., Pröebstle, M. and Martin, É. (2023), "Effect of laser contour scan parameters on fatigue performance of A20X fabricated by laser powder bed fusion", *International Journal of Fatigue*, Vol. 175, p. 107775.
- Kerstens, F., Cervone, A. and Gradl, P. (2021), "End to end process evaluation for additively manufactured liquid rocket engine thrust chambers", *Acta Astronautica*, Vol. 182, pp. 454-465.
- Kim, F.H. and Moylan, S.P. (2018), "Literature review of metal additive manufacturing defects", NIST.
- Kruth, J.-P., Leu, M.C. and Nakagawa, T. (1998), "Progress in additive manufacturing and rapid prototyping", CIRP Annals, Vol. 47 No. 2, pp. 525-540.
- Kumbhar, N.N. and Mulay, A.V. (2018), "Post processing methods used to improve surface finish of products which are manufactured by additive manufacturing technologies: a review", *Journal of The Institution of Engineers (India): Series C*, Vol. 99 No. 4, pp. 481-487.
- Leach, R. (2011), ed., *Optical Measurement of Surface Topography*, Springer Berlin Heidelberg, Berlin, Heidelberg.
- Leal, R., Barreiros, F.M., Alves, L., Romeiro, F., Vasco, J.C., Santos, M. and Marto, C. (2017), "Additive manufacturing tooling for the automotive industry", *The International Journal of Advanced Manufacturing Technology*, Vol. 92 Nos 5/8, pp. 1671-1676.
- Lesyk, D.A., Martinez, S., Mordyuk, B.N., Dzhemelinskyi, V. V., Lamikiz, A. and Prokopenko, G.I. (2020), "Post-Processing of the Inconel 718 alloy parts fabricated by selective laser melting: effects of mechanical surface treatments on surface topography, porosity, hardness and

Volume 31 · Number 1 · 2025 · 200–217

- residual stress", Surface and Coatings Technology, Vol. 381, p. 125136.
- Li, R., Liu, J., Shi, Y., Wang, L. and Jiang, W. (2012), "Balling behavior of stainless steel and nickel powder during selective laser melting process", *The International Journal of Advanced Manufacturing Technology*, Vol. 59 Nos 9/12, pp. 1025-1035.
- Lou, S., Jiang, X., Sun, W., Zeng, W., Pagani, L. and Scott, P.J. (2019), "Characterisation methods for powder bed fusion processed surface topography", *Precision Engineering*, Vol. 57, pp. 1-15.
- Mahboob Kanafi, M. and Tuononen, A.J. (2017), "Top topography surface roughness power spectrum for pavement friction evaluation", *Tribology International*, Vol. 107, pp. 240-249.
- Maleki, E., Bagherifard, S., Bandini, M. and Guagliano, M. (2021), "Surface post-treatments for metal additive manufacturing: progress, challenges, and opportunities", *Additive Manufacturing*, Vol. 37, p. 101619.
- Mate, C.M. and Carpick, R.W. (2019), Tribology on the Small Scale: A Modern Textbook on Friction, Lubrication, and Wear, Oxford University Press, Oxford (UK).
- Mohammadian, N., Turenne, S. and Brailovski, V. (2018), "Surface finish control of additively-manufactured Inconel 625 components using combined chemical-abrasive flow polishing", *Journal of Materials Processing Technology*, Vol. 252, pp. 728-738.
- Nakayama, K. and Hashimoto, H. (1995), "Experimental investigation of the superfinishing process", *Wear*, Vol. 185 Nos 1/2, pp. 173-182.
- Narasimharaju, S.R., Liu, W., Zeng, W., See, T.L., Scott, P., Jiang, X. (and Lou, S. (2021), "Surface texture characterization of metal selective laser melted part with varying surface inclinations", *Journal of Tribology*, Vol. 143 No. 5, p. 051106.
- Newell, D.J., O'Hara, R.P., Cobb, G.R., Palazotto, A.N., Kirka, M.M., Burggraf, L.W. and Hess, J.A. (2019), "Mitigation of scan strategy effects and material anisotropy through supersolvus annealing in LPBF IN718", *Materials Science and Engineering: A*, Vol. 764, p. 138230.
- Newton, L., Senin, N., Gomez, C., Danzl, R., Helmli, F., Blunt, L. and Leach, R. (2019), "Areal topography measurement of metal additive surfaces using focus variation microscopy", *Additive Manufacturing*, Vol. 25, pp. 365-389.
- Özel, T., Altay, A., Kaftanoğlu, B., Leach, R., Senin, N. and Donmez, A. (2019), "Focus variation measurement and prediction of surface texture parameters using machine learning in laser powder bed fusion", *Journal of Manufacturing Science and Engineering*, Vol. 142 No. 1, p. 011008.
- Paraschiv, A., Matache, G., Constantin, N. and Vladut, M. (2022), "Investigation of scanning strategies and laser remelting effects on top surface deformation of additively manufactured in 625", *Materials*, Vol. 15 No. 9, p. 3198.
- Pawar, G., Pawlus, P., Etsion, I. and Raeymaekers, B. (2012), "The effect of determining topography parameters on analyzing elastic contact between isotropic rough surfaces", *Journal of Tribology*, Vol. 135 No. 1, p. 011401.
- Peng, X., Kong, L., Fuh, J.Y.H. and Wang, H. (2021), "A review of post-processing technologies in additive manufacturing", *Journal of Manufacturing and Materials Processing*, Vol. 5 No. 2, p. 38.

- Puppi, D. and Chiellini, F. (2020), "Biodegradable polymers for biomedical additive manufacturing", *Applied Materials Today*, Vol. 20, p. 100700.
- Pyka, G., Kerckhofs, G., Papantoniou, I., Speirs, M., Schrooten, J. and Wevers, M. (2013), "Surface roughness and morphology customization of additive manufactured open porous Ti6Al4V structures", *Materials*, Vol. 6 No. 10, pp. 4737-4757.
- Raeymaekers, B. (2022), Design of Mechanical Elements: A Concise Introduction to Mechanical Design Considerations and Calculations, John Wiley & Sons, Hoboken NJ (USA).
- Raeymaekers, B. and Talke, F.E. (2010), "The effect of laser polishing on fretting wear between a hemisphere and a flat plate", *Wear*, Vol. 269 Nos 5/6, pp. 416-423.
- Reijonen, J., Revuelta, A., Riipinen, T., Ruusuvuori, K. and Puukko, P. (2020), "On the effect of shielding gas flow on porosity and melt Pool geometry in laser powder bed fusion additive manufacturing", *Additive Manufacturing*, Vol. 32, p. 101030.
- Sendino, S., Martinez, S., Lartategui, F., Gardon, M., Lamikiz, A. and Gonzalez, J.J. (2023), "Effect of powder particle size distribution on the surface finish of components manufactured by laser powder bed fusion", *The International Journal of Advanced Manufacturing Technology*, Vol. 124 Nos 3/4, pp. 789-799.
- Senthilnathan, A., Acar, P. and Raeymaekers, B. (2023), "Reconstructing synthetic surface topography maps from an experimental measurement using a Markov random field graphical network", *Tribology Letters*, Vol. 71 No. 3, p. 85.
- Seo, J., Rao, P. and Raeymaekers, B. (2023), "Generating synthetic as-built additive manufacturing surface topography using progressive growing generative adversarial networks", *Friction*, Vol. 12 No. 6, pp. 1283-1298.
- Singh, S. and Ramakrishna, S. (2017), "Biomedical applications of additive manufacturing: present and future", *Current Opinion in Biomedical Engineering*, Vol. 2, pp. 105-115.
- Snyder, J.C. and Thole, K.A. (2020), "Understanding laser powder bed fusion surface roughness", Journal of Manufacturing Science and Engineering, Vol. 142 No. 7, p. 071003.
- Strano, G., Hao, L., Everson, R.M. and Evans, K.E. (2013), "Surface roughness analysis, modelling and prediction in selective laser melting", *Journal of Materials Processing Technology*, Vol. 213 No. 4, pp. 589-597.
- Tian, Y., Tomus, D., Rometsch, P. and Wu, X. (2017), "Influences of processing parameters on surface roughness of Hastelloy X produced by selective laser melting", *Additive Manufacturing*, Vol. 13, pp. 103-112.
- Tian, Z., Zhang, C., Wang, D., Liu, W., Fang, X., Wellmann, D., Zhao, Y. and Tian, Y. (2020), "A review on laser powder bed fusion of Inconel 625 Nickel-Based alloy", Applied Sciences, Vol. 10 No. 1, p. 81.
- Tillmann, W., Schaak, C., Nellesen, J., Schaper, M., Aydinöz, M.E. and Hoyer, K.-P. (2017), "Hot isostatic pressing of IN718 components manufactured by selective laser melting", Additive Manufacturing, Vol. 13, pp. 93-102.
- Townsend, A., Senin, N., Blunt, L., Leach, R.K. and Taylor, J. S. (2016), "Surface texture metrology for metal additive manufacturing: a review", *Precision Engineering*, Vol. 46, pp. 34-47.

Volume 31 · Number 1 · 2025 · 200–217

- Valente, E.H., Gundlach, C., Christiansen, T.L. and Somers, M.A.J. (2019), "Effect of scanning strategy during selective laser melting on surface topography, porosity, and microstructure of additively manufactured Ti-6Al-4V", *Applied Sciences*, Vol. 9 No. 24, p. 5554.
- Vasco, J.C. (2021), "Chapter 16 additive manufacturing for the automotive industry", *Additive Manufacturing*, in Pou, J., Riveiro, A. and Davim, J.P. (Eds), Elsevier, pp. 505-530.
- Watring, D.S., Carter, K.C., Crouse, D., Raeymaekers, B. and Spear, A.D. (2019), "Mechanisms driving high-cycle fatigue life of as-built Inconel 718 processed by laser powder bed fusion", *Materials Science and Engineering: A*, Vol. 761, p. 137993.
- Whip, B., Sheridan, L. and Gockel, J. (2019), "The effect of primary processing parameters on surface roughness in laser powder bed additive manufacturing", *The International Journal of Advanced Manufacturing Technology*, Vol. 103 Nos 9/12, pp. 4411-4422.

- Xu, J., Ma, T., Peng, R.L. and Hosseini, S. (2021), "Effect of post-processes on the microstructure and mechanical properties of laser powder bed fused IN718 superalloy", *Additive Manufacturing*, Vol. 48, p. 102416.
- Yang, T., Liu, T., Liao, W., MacDonald, E., Wei, H., Chen, X. and Jiang, L. (2019), "The influence of process parameters on vertical surface roughness of the AlSi10Mg parts fabricated by selective laser melting", *Journal of Materials Processing Technology*, Vol. 266, pp. 26-36.
- Yasa, E., Poyraz, O., Solakoglu, E.U., Akbulut, G. and Oren, S. (2016), "A study on the stair stepping effect in direct metal laser sintering of a Nickel-Based superalloy", *Procedia CIRP*, Vol. 45, pp. 175-178.

Corresponding author

Bart Raeymaekers can be contacted at: bart.raeymaekers@vt.edu